ARTICLE

Check for updates

Nearby fault interaction within the double-vergence suture in eastern Taiwan during the 2022 Chihshang earthquake sequence

Chi-Hsien Tang [1], Yunung Nina Lin [1✉], Hsin Tung [1], Yu Wang [2], Shiann-Jong Lee[1], Ya-Ju Hsu [1], J. Bruce H. Shyu [2], Yu-Ting Kuo [3] & Horng-Yue Chen [1]

Nearby faults interact through stress changes induced by fault slip and viscoelastic flow. The process is, however, often elusive and can be geometry-dependent and time-variant. Here, we combine geodetic and field observations to characterize the interaction of two head-to-head, conjugate faults in eastern Taiwan during the 2022 Chihshang earthquake sequence. We map the coseismic slip on the Central Range fault and dynamically-triggered shallow slip on the Longitudinal Valley fault, which has been creeping interseismically. Overlapping of seismic and aseismic slip suggests that the Longitudinal Valley fault is capable of hosting a variety of distinct slip behaviors. Moreover, substantial slip on the Central Range fault suppresses Coulomb stress on the Longitudinal Valley fault, and vice versa, resulting in seismic bursts in an out-of-phase pattern on the two faults as seen in the hundred-year historical records. Such fault interaction implies the need for time-dependent seismic hazard reassessment for the complex fault system.

[1] Institute of Earth Sciences, Academia Sinica, Taipei, Taiwan. [2] Department of Geosciences, National Taiwan University, Taipei, Taiwan. [3] Department of Earth and Environmental Sciences, National Chung Cheng University, Chiayi, Taiwan. ✉email: ninalin@earth.sinica.edu.tw

Nearby fault interaction, a process critical for seismic hazard analysis, depends on the regional tectonic stress fields and the geometric setting of the faults. In crustal thrust fault systems, an earthquake on a fault may induce seismic events on a different fault segment within the same thrust sheet[1–3], stepping over to another thrust sheet[3–5], and/or down to the low-angle detachment[3]. Ruptures on shallow minor structures may also be triggered at the same time[5,6]. Of all geometric settings, the interaction between two major head-to-head, conjugate thrust faults has the least known cases—the only well-documented example is probably the south-vergent San Fernando fault and the north-vergent Oak Ridge fault in the Los Angeles region, which produced the 1971 M7.1 San Fernando earthquake and the 1994 M6.8 Northridge earthquake, respectively[7–12]. Before the 1971 earthquake, there were no recorded major earthquakes along the fault system, except for a possible one in 1812[12,13]. Given the low slip rates of faults and the long recurrence interval for large rupture events[12–14], observing the rupture scenario and near-field fault interaction might be challenging during our lifetime. However, a recent earthquake sequence in eastern Taiwan, along with high tectonic shortening rates and frequent earthquakes, may provide insights into fault interactions between two head-to-head, conjugate thrust faults.

The September 2022 Chihshang earthquake sequence includes two major shallow earthquakes in eastern Taiwan. The first one is a moment magnitude (M_w) 6.5 foreshock on September 17, followed by an M_w 7.0 mainshock 7 km to the north and 17 h later on September 18 (moment magnitudes from autoBATS CMT, https://bats.earth.sinica.edu.tw/). These two earthquakes occurred within the narrow and elongated Longitudinal Valley, an active suture zone between the Luzon Arc on the Philippine Sea Plate to

the east and the accretionary wedge of the Taiwan Orogeny along the Eurasian continental margin to the west (Fig. 1a). Global Navigation Satellite System (GNSS) observations show that around 30 out of the total 90 mm yr^{-1} northwestward plate convergence is absorbed across the valley[15]. Within the suture, the east-dipping, sinistral strike-slip Longitudinal Valley fault (LVF) is considered the main plate boundary fault located along the eastern edge of the valley[16] (Fig. 1b). Several M_w 6.7–7.3 earthquakes have been documented along this fault during the past one hundred years[17]. Beneath the western side of the valley, although the west-dipping Central Range fault (CRF) has been proposed, its activity has been questioned due to its proximity to the LVF[18–21] (Fig. 1b and S1). Although a magnitude ~7 earthquake may have possibly occurred on the CRF (north of 23.5°N) in 1908[17,22,23], the CRF south of 23.5°N, unlike the neighboring LVF section, has shown no notable creeping[24–26] and has remained seismically inactive for nearly a century. The quiescence is eventually ended by a series of moderate earthquakes that began in 2006[27] and culminated in the 2022 Chihshang earthquake sequence.

The 2022 earthquakes are located to the west of the Longitudinal Valley, with the mainshock close to the town of Chihshang (Fig. 1d). This event demonstrates that the CRF accommodates also present-day plate boundary shortening, and that the LVF and CRF together form an active head-to-head, conjugate fault system (Fig. 1b), similar to the San Fernando fault and the Oak Ridge fault in southern California. With this unique opportunity, we use seismic, geodetic, and field geologic records to study the interaction between the CRF and LVF during and after the 2022 earthquakes, as well as to evaluate the first-order moment budgets on the two faults over the past ~120 years.
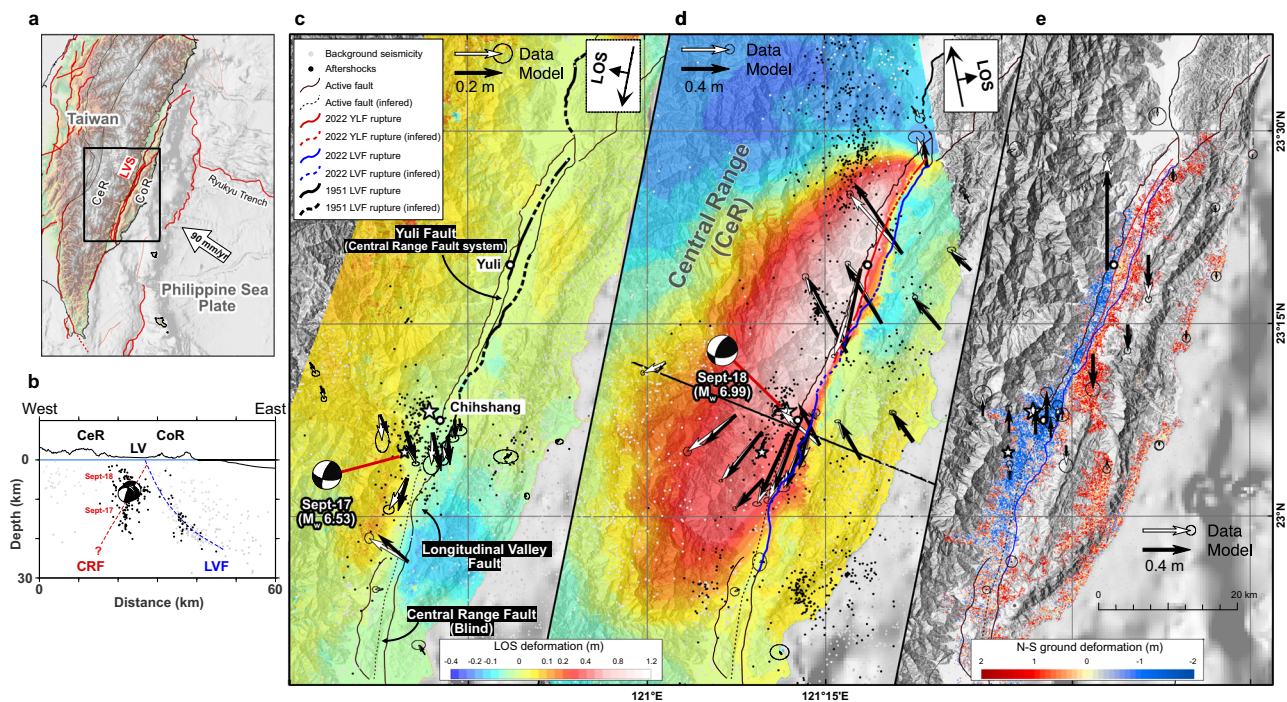
Fig. 1 Surface displacements of the September 2022 Chihshang earthquake sequence. a Tectonic setting of the Longitudinal Valley suture zone (LVS). CeR: Central Range; CoR: Coastal Range. **b** Cross section view showing the distribution of background seismicity between 1990 and 2020 (light gray dots)[55]. Relocated aftershocks prior to November 17 are in black dots (catalog from Taiwan Geophysical Database Management System, Taiwan GDMS, https://gdmsn.cwb.gov.tw/). See (**d**) for profile location. **c** Coseismic interferogram and GNSS horizontal displacements for the foreshock[56]. Traces of the Central Range fault and the Longitudinal Valley fault (LVF) are based on the Taiwan Earthquake Model[31]. Traces of the 1951 surface ruptures on the Yuli fault (YLF) and the LVF are based on previous field surveys[28,29]. LOS: radar line-of-sight direction. **d** Coseismic interferogram and GNSS horizontal displacements for the mainshock. **e** Cumulative N–S offsets from the foreshock to the mainshock. Vectors represent the GNSS vertical coseismic displacement for the mainshock.
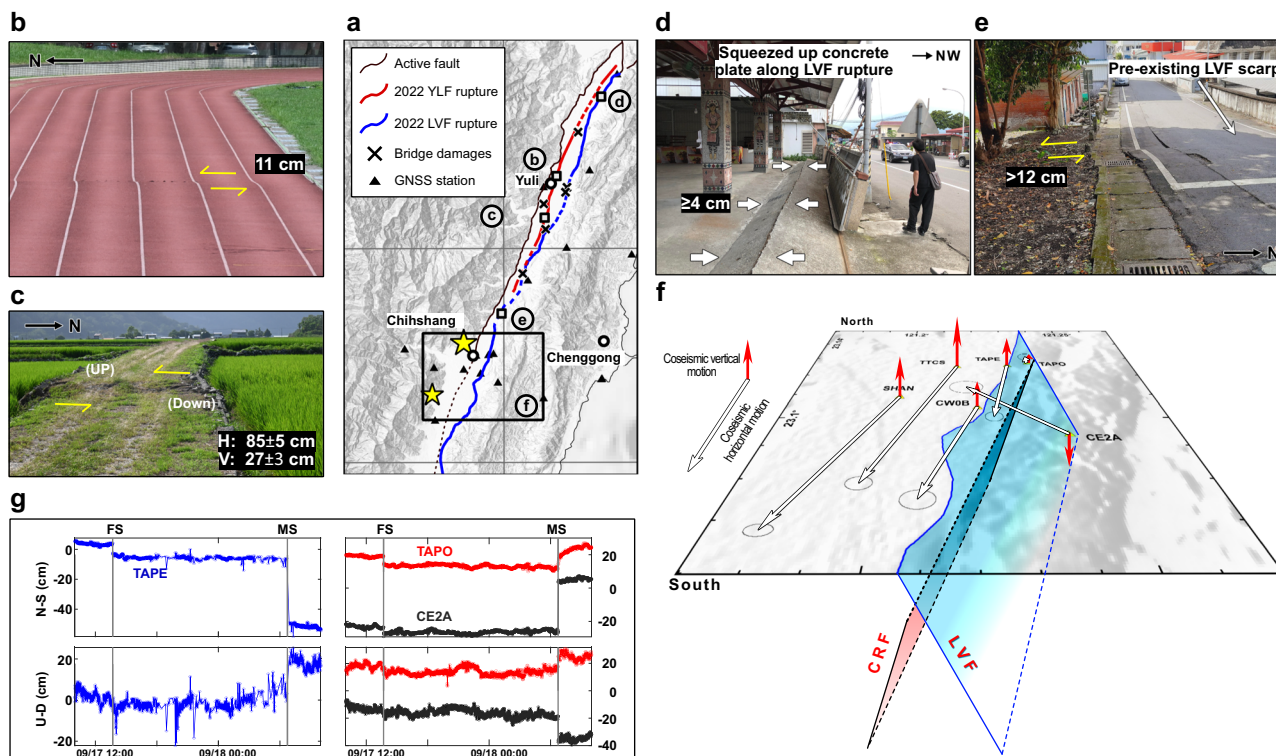
Fig. 2 Field photos and geodetic observations of the ruptures along the CRF and LVF. a Map showing locations of the surface ruptures and field photos along (**b**, **c**) the CRF and (**d**, **e**) the LVF. **f** Coseismic GNSS displacements for the mainshock near Chihshang. **g** North and vertical component of the GNSS position time series at station TAPE (30 m west of the LVF), TAPO (540 m east of the LVF) and CE2A (2.3 km east of the LVF)[56]. FS foreshock, MS mainshock. The northward and upward coseismic motion of TAPO during the mainshock deviates from the motions of other stations in the hanging wall of the CRF (with southwestward and upward coseismic motion), as well as CE2A located further east (with northwestward and downward coseismic motion). This anomalous motion suggests the near-field interference from the LVF, most likely a coseismic shallow slip.

Results

Surface rupture and displacement field. Field survey immediately after the mainshock shows that most of the surface ruptures occurred 15-km north of the epicenter, close to the town of Yuli (Figs. 1 and 2). The rupture traces are 1–2 km east of the previously mapped CRF along the Yuli fault, which was first identified by minor surface ruptures during the 1951 M_w 7 earthquake[17,28,29] (Fig. 1c). The Yuli fault used to be considered as an *en echelon* stepover of the LVF[28], but now we reattribute it to the larger CRF system (with "system" omitted hereafter for simplicity). Notable left-lateral and vertical offsets (west side up) are observed in this section (Fig. 2b, c), whereas to the south near the epicenter, field survey shows only diffuse deformation without noticeable offsets. On the LVF, minor fractures are distributed all the way from north to south showing left-lateral motions and horizontal shortening in places (Fig. 2a, d, e). These field ruptures are comparable to the results from optical image pixel offset tracking using Sentinel-2 images: the sharp 2-m N–S offset in the north diminishes southwards, and the offset discontinuity moves eastwards towards the surface trace of the LVF (Fig. 1e). The topographic relief in the mountain ranges on both sides of the valley limits the resolvable pixel offsets away from the fault, so interferometric synthetic aperture radar (InSAR) images acquired by the L-band Advanced Land Observing Satellite-2 (ALOS-2) provide additional constraints for the coseismic deformation (Fig. 1c, d). The ground displacement during the foreshock displays an anti-symmetric pattern across the fault. During mainshock, the ground west of the CRF has moved ~1 m towards the satellite, while the ground to the east has moved ~0.1 m away from the satellite. This asymmetric pattern indicates reverse motion along a west-dipping fault plane, compatible with the field

observations and focal mechanisms (Fig. 1d; solutions from the Real-Time Moment Tensor Monitoring System[30], https://rmt. earth.sinica.edu.tw/). The foreshock and the mainshock hypocenters are each located at the northern and southern edge of the corresponding deformation patches, suggesting bilateral rupturing processes that occur sequentially with a 17-hr time delay.

More than 30 GNSS stations operate continuously along the Longitudinal Valley. During the foreshock, a dense GNSS array near Chihshang displays a sharp change of N–S displacements from the hanging wall to the footwall of the CRF (Fig. 1c). During the mainshock, the coseismic horizontal and vertical displacements west of the CRF reach 0.65 m and 0.95 m, respectively (Fig. 1d, e). East of the CRF, the maximum horizontal displacement also reaches 0.72 m, with the maximum ground subsidence of 0.37 m. Along the dense GNSS array near Chihshang, station TAPE and TAPO, which are ~570 m apart across the LVF, show opposite horizontal motions during the mainshock (Fig. 2f, g). Such a short-wavelength deformation, together with surface ruptures observed along the LVF (Fig. 2a, d, e), indicates that the mainshock of the Chihshang earthquake sequence may trigger the shallow slip on the LVF.

Coseismic slip and rupture process. Given that surface ruptures are observed both along the CRF and LVF faults, the fault model is designed with a west-dipping plane for the CRF, with a uniform dip angle of 60° according to the focal mechanism, and an east-dipping fault plane, with its listric geometry and surface trace following the parameters for the LVF in the Taiwan Earthquake Model (TEM)[31]. In the northern section near Yuli, the surface trace of the CRF follows the observed ruptures and the discontinuity in pixel offset tracking results (Fig. 1e). Due to the lack of surface ruptures in the southern section of the CRF, we
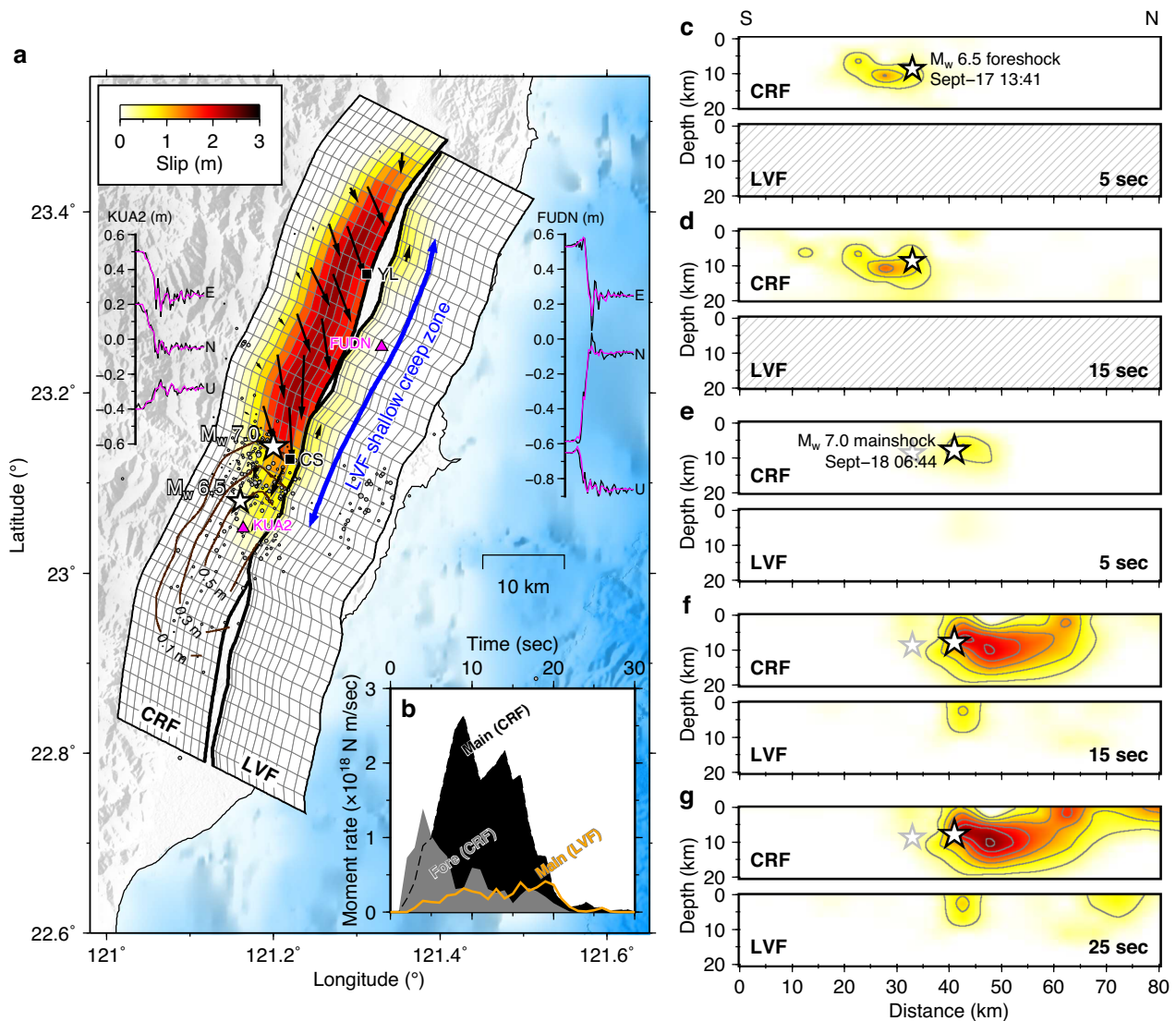
Fig. 3 Coseismic slip during the September 2022 Chihshang earthquake sequence. a Overview of the kinematic model constrained from satellite imagery and GNSS coseismic displacements[56]. Brown contours and colored patches represent the slip during the foreshock and mainshock, respectively. Gray circles are aftershocks between the foreshock and mainshock. YL: Yuli. CS: Chihshang. **b** Source time functions obtained from the rupture process modeling constrained by HR-GNSS data. Gray and black plots represent the foreshock and the mainshock on the CRF, respectively, whereas orange curve shows contributions of the LVF during the mainshock. Records from two of the HR-GNSS sites (KUA2 and FUDN) are shown in (**a**). Black and magenta curves are observed and modeled records. **c**, **d** Rupture process for the foreshock. Hatched areas indicate the fault plane excluded from the inversion. **e–g** Rupture process for the mainshock.

leverage the planar fault constrained by coseismic displacements during the foreshock (e.g., GNSS and InSAR) to determine the location of the CRF there (Fig. S7). The result suggests that the up-dip end of the CRF submerges under the LVF south of Chihshang, which is in agreement with the eastward shift of the discontinuity in the interferogram and N–S displacement field (Fig. 1d, e).

We use satellite imagery and GNSS displacements to constrain the coseismic slip distribution on the two faults (Fig. 3a). We carry out various model scenarios showing that the coseismic displacements during the foreshock can be adequately explained by the CRF alone, whereas the coseismic displacements during the mainshock may require both the CRF and LVF (see Figs. S10–S15 and Tables S1–S2 for a complete set of different model scenarios). We perform synthetic tests (Fig. S18) and examine model uncertainties using the standard deviation estimated through error propagation (Fig. S19) to ensure that the performance of our

model is sufficient to support the following discussions. During the foreshock, most of the slip occurs to the south of the foreshock hypocenter. During the mainshock, the rupture forms two major asperities: the first one is right to the north of the epicenter at a depth of 5–15 km; the second asperity starts further north from a greater depth and extends to the surface north of Yuli. The slip peaks at ~2.4 m, with an average rake of 53°. The total slip from the foreshock to the mainshock forms a contiguous patch over 60 km long on the CRF. On the LVF, minor and predominantly left-lateral slip takes place mostly at the shallow depth (<5 km) near Chihshang during the mainshock. Our model also indicates another shallow slip patch on the LVF near Yuli. Although there is no direct evidence from nearby GNSS stations like those near Chihshang, two bridges near Yuli were damaged due to substantial surface offset along the LVF (Fig. 2a).

To better understand the rupture process, we employ 1-Hz sampling high-rate GNSS (HR-GNSS) position time series to

invert the spatiotemporal evolution of slip. Kinematic and static coseismic displacements from HR-GNSS data are both used to constrain the inversion. The result shows that the rupture on the CRF predominantly propagates southwards during the foreshock and terminates at ~5 km depth (Fig. 3c, d). The relatively subtle shallow slip in the kinematic rupture is slightly different from the static slip jointly imaged by GNSS and InSAR data (Fig. 3a), which provides more constraints on the shallow slip on the CRF. About 17 h later, the mainshock rupture initiated close to where the foreshock rupture terminated and propagated unilaterally northwards, accompanied by the shallow ruptures on the LVF between Chihshang and Yuli (Fig. 3e, g). The seismic moment release estimated from the two aforementioned modeling strategies is $5.7–9.7 \times 10^{18}$ N·m (equivalent to M_w 6.4–6.6) for the foreshock and $3.3–3.6 \times 10^{19}$ N·m (equivalent to M_w 7.0) for the mainshock. This rupture process inverted from HR-GNSS datasets appears to be similar to that obtained from teleseismic and local strong motion waveforms[32], which also include constraints from GNSS static coseismic displacements. Our result thus demonstrates that the HR-GNSS data in eastern Taiwan have the ability to independently image seismic rupture processes.

Discussion

Slip behaviors on the CRF and LVF. The 2022 Chihshang earthquake sequence gives us a glimpse into the slip behaviors on the long-debated CRF. To study the variation of slip behaviors along the down-dip direction, we model the GNSS postseismic displacements within the first 34 days following the earthquake as afterslip to obtain the approximate spatial distribution (see Fig. S17 and Table S3 for scenario tests between single and dual faults). The result shows subtle to none afterslip at the up-dip side of the CRF rupture zone despite the apparent coseismic shallow slip deficit (Fig. 4). However, we caution that the lack of shallow afterslip may as well result from sparse GNSS distribution close to the CRF north of Chihshang. On the other hand, notable shallow afterslip occurs on the LVF near Chihshang. This contrast may be related to lithological differences between the LVF and CRF, which are characterized by a younger, non-metamorphic mélange and an older, metamorphic complex, respectively[33]. The down-dip side of the CRF rupture zone is bounded by afterslip of ~0.8 m extending to a depth of 30 km (Fig. 4). The deep postseismic slip is mostly located in the aseismic zone beneath the southeastern Central Range, where ductile deformation is presumably prevalent due to high heat flow and low viscosity[34,35]. Only a few aftershocks were recorded in this region within two months of the earthquake, suggesting that viscoelastic flow may play an essential role in postseismic deformation in the vicinity of the fault and from this depth downwards. Therefore, part of the inverted afterslip may be a proxy of the viscoelastic flow excited by the deviatoric stress changes after the earthquakes. Note that the southern end of the afterslip patch seems to have a larger amount of slip, which is possibly a result of uneven station distribution. Incorporating InSAR observations may help verify this anomaly.

On the LVF, the shallow part has been creeping steadily at high rates[19,36,37] and experienced coseismically-induced slip during the mainshock. Postseismic GNSS observations and modeling suggest that afterslip also occurs close to the surface near Chihshang (Fig. 4), despite a Coulomb stress drop of ~1 MPa after the earthquake (Fig. 5c). The fact that slip can occur on the shallow part of the LVF during different stages of the earthquake cycle is rather unique and perplexing. It implies that more strain is released during and after the earthquake, even though the strain is being released constantly in the interseismic period. This phenomenon suggests that the shallow part of the LVF is likely a
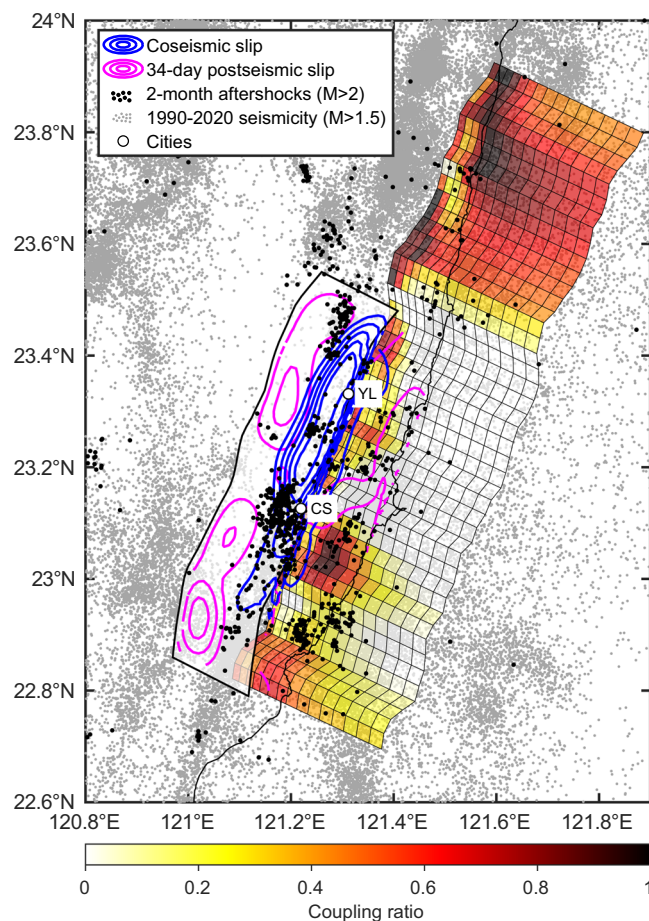

Fig. 4 Coseismic slip (during the foreshock and mainshock) and early afterslip (34 days after the mainshock) of the 2022 Chihshang earthquake sequence. Contour interval is 0.4 m on the CRF and 0.1 m on the LVF. The fault plane has been extended to 30 km at depth for the afterslip inversion. The interseismic coupling (ISC) model was constructed by using InSAR and GNSS observations with the geometry of the LVF only[37]. Gray dots are relocated background seismicity (M > 1.5) between 10 and 30 km, 1990–2020[55]. Thick black dots are aftershocks (M > 2) between September 18 and November 17 from Taiwan GDMS. YL: Yuli. CS: Chihshang.

frictionally transition zone, which is a conditionally stable region[38] that can also promote the propagation of seismic ruptures depending on the stress and physical conditions[39]. Studies have shown strong ground shaking during large events may potentially change the elastic and frictional properties in the fault zone[40]. Under what exact conditions the shallow part can undergo all-time slip requires further explorations from laboratory experiments and numerical simulations.

A previous geodetically-determined interseismic coupling (ISC) model for the LVF indicates intermediate coupling at the shallow part and low coupling at the deeper part near Yuli[37] (Fig. 4). The spatial extent and strike (N20°E) of the shallow coupling patch agree well with those of the 2022 coseismic slip patch, suggesting that the ISC model has indeed captured the elastic strain associated with fault coupling, albeit the main source is the CRF. The actual coupling for the LVF, from shallow to deep, is therefore in question given the nearby influence from the CRF. In addition to geometric unknowns (single vs. dual faults as well as fault intersections), the short geodetic baselines in the Longitudinal Valley may limit the resolution at depth. This limitation highlights the necessity for offshore geodetic data to
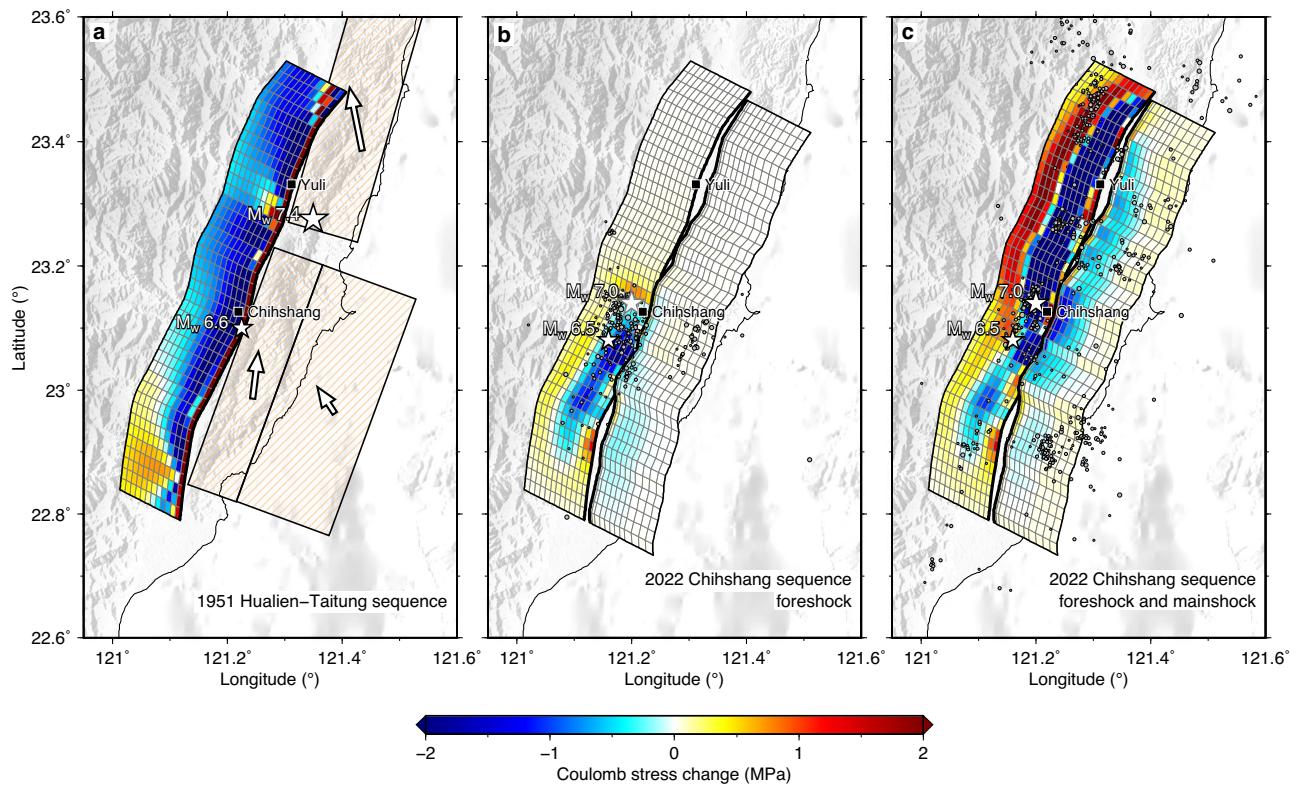
Fig. 5 Coulomb stress change after the 1951 and 2022 earthquake sequence. a Coulomb stress change on the CRF imparted by the slip on the LVF (slip model from ref. [16]) during the 1951 earthquake sequence. **b** Coulomb stress changes due to the slip in the September 2022 foreshock. Gray circles are aftershocks between the foreshock and mainshock. **c** Coulomb stress changes due to the slip in the mainshock. Gray circles are the aftershocks after the mainshock. A rake of 45° is adopted for the CRF and LVF as a receiver fault. The friction is assumed to be 0.4[54]. Note the Coulomb stress decrease on one fault due to the slip on the other. Earthquake catalog is from Taiwan GDMS.

enhance the accuracy and resolution of ISC analysis on faults in eastern Taiwan.

Nearby fault interaction during earthquakes. The spatial proximity of the CRF and LVF leads to intense and complicated interactions during seismic events. The moment release on the LVF is $3.2–4.9 \times 10^{18}$ N·m in the mainshock, accounting for 9–15% of the total moment release. According to the source time functions for the mainshock (Fig. 3b), the moment release rate on the CRF rose quickly, peaked at 9 s, and decreased stepwise till 30 s. The moment release on the LVF started 2–3 s later, increased gradually all the way till 20 s, followed by a sharp drop at 20–23 s and another tiny peak at 25–26 s. The slightly-delayed onset of moment release on the LVF suggests that the shallow slip was dynamically triggered by seismic waves, most likely by the strong S wave or Rayleigh wave[39]. The long duration for the induced slip on the LVF is particularly intriguing. The slip even picked up more momentum during the later phase of the mainshock between 15 and 20 s while the moment release on the CRF has already decreased from the peak. One possible explanation is a larger excitation when the S wave or the surface wave from the second asperity traveled northeastwards across the LVF. In view of dual ruptures, the same phenomenon has been recorded previously during the 1951 earthquake, in which the LVF hosted the main slip (Fig. 1c). The records from both the 1951 and 2022 earthquakes suggest that the CRF and LVF are likely to rupture simultaneously during major earthquakes ($M_w > 7$), with the faults alternating between the primary and the secondary structures. Such a tendency needs to be considered when evaluating the energy budget of seismic events.

Static stress changes in a closely-spaced fault system. As what would be expected from the perspective of typical Coulomb stress transfer, the ruptures on the CRF during the foreshock caused a Coulomb stress increase by 0.5 MPa to the northern edge of the slip patch, which then led to a sequence of aftershocks and eventually the mainshock (Fig. 5b). After the mainshock, a ring of increased Coulomb stress circled the coseismic slip patch on the CRF, with the stress increase up to 2 MPa at the up-dip and down-dip ends. On the LVF, however, a continuous patch with stress reduction extends through the entire fault section at 2–20 km depth, with the maximum decrease of 1 MPa near the hypocenter (Fig. 5c). This large stress drop suggests that the seismic potential on the LVF may be impeded, at least in principle, subsequent to the 2022 earthquakes.

Similarly, the 1951 coseismic ruptures[16] induced a Coulomb stress drop of 1–2 MPa on the CRF (Fig. 5a). Although these values may be overestimated given the uncorrected postseismic effects, the pattern and sign of stress changes can still be instructive. They correspondingly suggest that the seismicity on the CRF may have been suppressed following the 1951 earthquakes.

The temporary shutdown of seismicity caused by slip on the other fault in a head-to-head, conjugate thrust fault system can also be found in historical earthquake records. When viewed from the entire length of 140 km (Fig. 6a), historical earthquakes since 1900 with magnitude larger than 6 and depth shallower than 30 km[17,23] show a period of quiescence following the occurrence of a major event on the other fault—a 37-year-long quiescence on the LVF after the 1908 M_w 7 earthquake on the CRF, and a 62-year-long quiescence on the CRF after the 1951 earthquake sequence on the LVF (Fig. 6b). A larger moment release on one
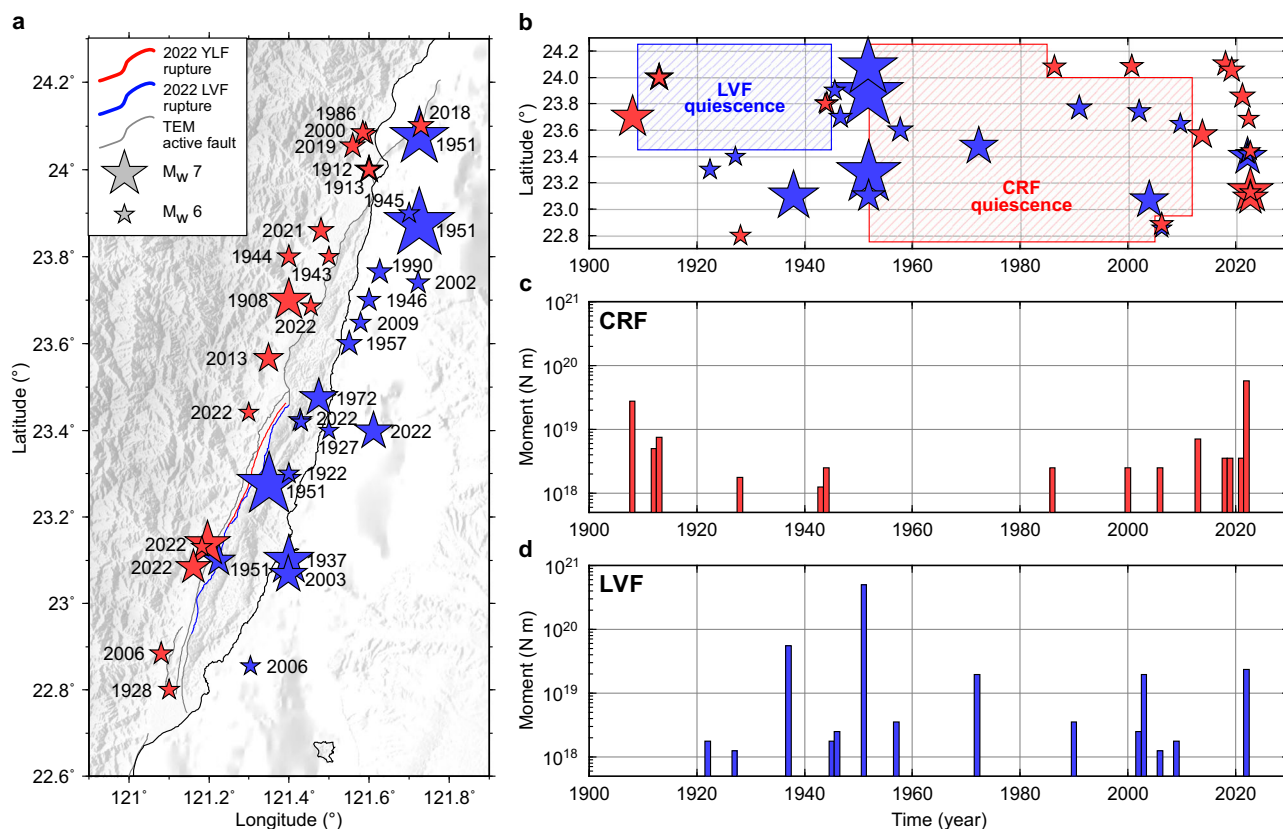
Fig. 6 Historical earthquake records in the Longitudinal Valley since 1900. a Spatial distribution of historical earthquakes since 1900 with $M > 6$ and depth <30 km[17,23]. Red and blue stars mark earthquakes attributed to the CRF and LVF, respectively. Red and blue lines are the 2022 surface ruptures along the Yuli fault and the LVF. Gray lines represent other active faults in the Taiwan Earthquake Model[31]. **b** Spatial and temporal distribution of historical earthquakes and the two quiescence periods. **c** Moment release by individual events on the CRF. **d** Moment release by individual events on the LVF.

fault likely results in a longer quiescence period on the other fault. This relationship agrees with the stress drop estimated after the 1951 and the 2022 earthquakes (Fig. 5). It also suggests that for a head-to-head, conjugate fault system with low slip rates, such as that in the Los Angeles region (~4 mm yr^{-1} for the San Fernando fault[12,13] and 3–12 mm yr^{-1} for the Oak Ridge fault[10,12] as compared to 29–38 mm yr^{-1} for the LVF and 6–11 mm yr^{-1} for the CRF; see Table S4), the stress drop imparted by an $M_w > 7$ earthquake on the nearby fault may lead to an even longer quiescence. This effect may take part in the centuries-long seismic lull in the Los Angeles area, especially in between the short-range thrust faults[12].

Arguably, as a result of the stress shadow effect, the moment releases on the CRF and LVF have trended out of phase over the past ~120 years (Fig. 6c, d). Such an out-of-phase pattern has also been reported over a larger spatiotemporal scale across different fault systems in Southern California[41] and in central Italy[42]. It is however the first time that the out-of-phase seismic bursts are reported along two major faults in a hundred-year time scale. In the long run, viscous flows in the lower crust may weigh in to add more complexity to the interaction between the faults and with other structural systems in the far range[42]. Further physics-based modeling will be needed to examine the stochastics and stationarity of the out-of-phase pattern.

Moment budgets and seismic risks. A large earthquake like the 2022 mainshock raises the question of how many more large events to be expected along the CRF and LVF. While a detailed ISC model may be preferred to answer such a question, such modeling has a large degree of freedom in this area: sparse GNSS stations in the

Central Range, poorly-constrained geometry of the CRF, and the limited spatial coverage of geodetic data around the Longitudinal Valley. Alternatively, we invoke centennial earthquake records and millennial geologic rates derived from deformed fluvial terraces to estimate a first-order moment budget for the two faults over the past ~120 years. The moment budget consists of moment accumulation and moment release. To estimate the moment accumulation, a 140-km × 30-km plane is assigned to represent the full length of each fault. The long-term slip rate $\dot{s}$ of 29.0–38.0 mm yr^{-1} and 6.7–11.0 mm yr^{-1} is assigned to the LVF[43,44] and the CRF[20,31], respectively, based on the long-term uplift of fluvial terraces on each side (Table S4). The accumulated moment can be estimated by using $\mu A \dot{s} \Delta t$, where μ is shear modulus (30 GPa), A is the fault area, and Δt is the year since 1900. The moment release can be estimated by summing up the seismic moments from major earthquakes (Fig. 6a) and the aseismic moment release from the shallow creeping zone on the LVF (Table S4). For simplicity, the moment budgets are set to zero at the previous large earthquakes, i.e., the 1951 earthquake sequence for the LVF and the 1908 earthquake sequence for the CRF (Fig. 7b). The result shows that the 2022 earthquake sequence seems to release most of the moments accumulated on the CRF since 1908. The estimated current budget is around -0.7–5.9×10^{19} N·m given the uncertainties in the long-term slip rate. The surplus can be accommodated by small historical events ($M < 6$) that are not accounted in the estimate, the postseismic transients, and/or the future earthquakes that fill up spatial gaps (Fig. 7a). Note that the spatial gap north of 23.75°N is surrounded by small rupture patches associated with M_w 6.1–6.4 earthquakes, and hence the gap may serve as a possible candidate to host future large earthquakes.
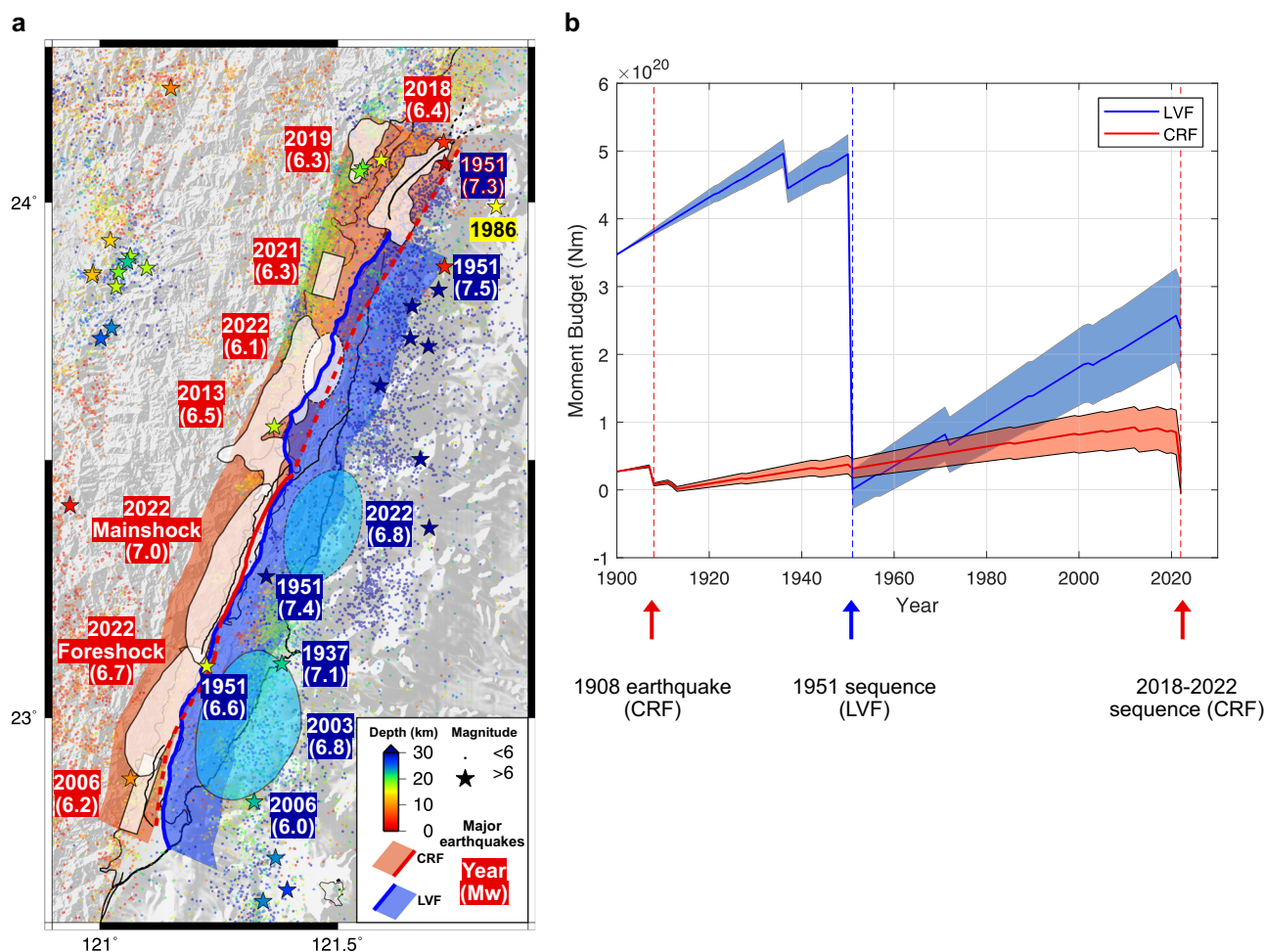
Fig. 7 Rupture patches and moment budget for the CRF and LVF. a Map view of the rupture patches for Mw > 6 earthquakes[27,57-61]. The northern extension of the CRF is based on the distribution of background seismicity[55] and rupture patches[61]. The up-dip end to the north and to the south is likely blind, overridden by the LVF. **b** Moment budget of the CRF and LVF. The uncertainty estimation comes from the uncertainties in long-term slip rates.

On the other hand, a considerable amount of moment has continued to accumulate on the LVF since 1951. The current budget, with the moment release from shallow interseismic creeping subtracted, is already 2–3 times the moment released by the 2022 earthquakes (Fig. 7b). The current surplus reaches $1.7–3.1 \times 10^{20}$ N·m, equivalent to an earthquake of M_w 7.4–7.6. On the map view, M_w 6–6.8 earthquakes have occurred sporadically along the deeper part of the LVF, while the shallow part (<10–15 km) has not experienced major seismic events since 1951 (Fig. 7a). Although smaller earthquakes and interseismic creeping may consume part of the accumulated moment, another series of major earthquakes with the same amount of moment release as the 1951 earthquake sequence is likely to take place within 45–84 years given the current budget accumulation trend.

The influence of stress shadow on the CRF and LVF imposed by the 1951 and 2022 earthquakes, respectively, is also included in the moment budget (see "Methods"). The stress shadow effect on the LVF's budget curve is difficult to visualize due to another M_w 6.8 earthquake in 2022, while the effect is visible on the CRF's budget curve as a small offset (Fig. 7b). This offset indicates a drop of stress level on the CRF and seismicity shutdown afterwards, as revealed in the post-1951 quiescence. Although this is a rough estimate, we show that nearby fault interaction may modulate the moment budget in a head-to-head, conjugate thrust fault system such as the CRF and LVF.

Summary

The presence of a head-to-head, conjugate thrust fault system along the Longitudinal Valley suture was not completely obscure given the historical earthquakes and the geomorphic evidence of the CRF. However, the system did not draw much attention in the past, partly due to the high activity exhibited by the LVF. The 2022 Chihshang earthquake sequence demonstrates that both the CRF and LVF accommodate plate convergence and are capable of generating earthquakes of M_w 7 or greater. Profound fault interaction during and after the earthquake has caused periods of quiescence and an out-of-phase temporal pattern of moment release between the two faults. This result not only urges us to revise the conventional thinking of plate convergence across eastern Taiwan, but also signals the importance of incorporating nearby fault interaction when assessing seismic hazards in similar tectonic settings. Future modeling needs to account for the geometric complexity, slip characteristics, and stress interactions between the faults in order to obtain realistic estimations.

Methods

Optical image correlation of Sentinel-2 image. Sentinel-2 level 2 A (L2A) data (https://doi.org/10.5270/S2_-znk9xsj) acquired between 2022/08/23 and 2022/09/22 are used to estimate the horizontal ground displacements associated with both the foreshock and the mainshock. The L2A product includes orthorectified blue (B2), green (B3) and red (B4) bands at 10-m spatial

resolution. To derive the ground displacement fields, the pre- and post-earthquake images were each converted to a gray-scale image using the linear combination of B2, B3 and B4 bands. The Co-registration of the Optically Sensed Images and Correlation (COSI-Corr) method[45] was used to retrieve the sub-pixel displacements between the two images. We utilized two window sizes, 64 × 64 pixels and 32 × 32 pixels, for the correlation, and set the sliding step to one pixel. The corresponding resolution for the displacement fields is 10 m. We set the robustness iteration to four and the frequency mask threshold to 0.98. The output of COSI-Corr includes three map layers: E–W, N–S displacement field and the signal-to-noise ratio (SNR) layer (Fig. S2). To further decrease the noise in E–W and N–S displacement fields, we apply the non-local mean filter with the noise parameter H set to 1.6. The final results are validated with the surface offsets collected from the field survey. Because of the high noise level and the small displacement values, we discard the E–W displacement field. The N–S offsets are then resampled using a quad-tree scheme based on the data SNR values and the local variances. A subset of ~2250 points are selected for the kinematic modeling.

ALOS-2 L-Band SAR interferometric data. L-band ALOS-2 PALSAR-2 SAR data in ScanSAR mode acquired on 2022/04/03 and 2022/09/18 from descending path 27 are used to produce the interferogram for the foreshock. The post-event image was acquired 6 h after the foreshock, so some post-seismic displacements are included in the image (Fig. S3). ALOS-2 SAR data in Stripmap Fine mode acquired on 2022/05/19 and 2022/09/22 from ascending path 137 are used to produce the interferogram for the mainshock. The post-event image was acquired 82 h after the mainshock. A different track, ascending path 139 was available ~10 h after the mainshock, but the images suffer strong ionospheric disturbance and were not able to provide as clear fringe patterns as those in path 137. The interferograms are produced using the standard Interferometric synthetic aperture radar Scientific Computing Environment package (ISCE2, https://github.com/isce-framework/isce2), with the embedded ionospheric correction module for L-band wide-swath SAR data[46]. The unwrapped interferograms are converted to line-of-sight (LOS) displacements. Because of low coherence in the mountain areas, multiple unwrapping errors are observed in the interferogram that covers the mainshock. We manually correct for the unwrapping errors and validate the results with the coseismic displacements from GNSS observations projected to the LOS directions (Fig. S4). The result shows a better agreement between the InSAR and the GNSS LOS displacements. The two interferograms are then resampled in a non-uniform scheme based on the coherence value and the local variances. Considering the loss of coherence and hence potential unwrapping errors due to large displacement gradient near the surface rupture, we exclude points within ±1 km of the fault traces. For the foreshock interferogram, we crop out the region contaminated by ionospheric noises and resample the data to 1028 points following a quad-tree scheme based on the data coherence and local variances. The mainshock interferogram is resampled to 5797 points using the same method.

Processing of high-rate GNSS data. Given that the foreshock and mainshock were less than a day apart, we collected 1-Hz GNSS observations in the study area to rigorously determine the coseismic displacements. The GipsyX/RTGx (Real Time GIPSY) software package[47] was used to estimate the coordinates in precise point positioning method with the precise final, non-fiducial daily products of orbit positions and clock offsets from the Jet Propulsion Laboratory archives. The Vienna Mapping Function[48]

and antenna calibration provided by the National Geodetic Survey in National Oceanic and Atmospheric Administration were used to reduce atmosphere delays and to carry out phase center modeling.

We estimated the GNSS coseismic displacements by using 1-Hz data. The coseismic displacement field of the foreshock was determined by using the difference between the 30-s average position immediately preceding the foreshock and the one spanning from the 30th to the 60th seconds after the foreshock onset. This is to avoid the influence of coseismic phase data on our calculation. The maximum horizontal displacement is measured in the station ERPN, with a southwestward horizontal displacement of ~0.19 m. Similar to the foreshock, the coseismic displacement field of the mainshock was determined by using the difference between the 1-minute average position immediately preceding the mainshock and the one spanning from the 1st to the 2nd minute. after the earthquake onset. The maximum horizontal displacement is measured in the station Yul1, with a SSW horizontal displacement of ~0.75 m and a vertical displacement of almost one meter. The locations and time series of all the high-rate GNSS sites used in the modeling are shown in Figs. S5 and S6.

For the postseismic displacements, we processed the position GNSS data within 34 days after the mainshock. The postseismic position time series $x(t)$ are fitted by the following function[35,49]:

$$x(t) = A\left\{1 - \frac{2}{k}\operatorname{arcosh}\left[\exp\left(\frac{\mathbf{t}}{t_c}\right)\coth\left(\frac{k}{2}\right)\right]\right\}, k > 0 \quad (1)$$

where A is the amplitude of postseismic transient, $\mathbf{t}$ is the time since mainshock, k is a dimensionless parameter related to the velocity-strengthening behavior of faults in response to stress changes, and t_c is a characteristic time scale of transient deformation. Here we use $k = 5.5$ and $t_c = 0.1$ years, determined by a grid search, to capture the rapid postseismic deformation.

Co-seismic and postseismic slip inversion. We include both the CRF and LVF in our model to image the coseismic slip (Fig. S7). In the inversion, we invert the foreshock coseismic displacements with the CRF solely, while the LVF is included to jointly explain the mainshock observations. For the CRF, the fault trace near Yuli is illustrated by the coseismic surface rupture along the Yuli fault (a branch of the CRF). The surface rupture of the Yuli Fault vanishes southwards due to the overriding of the LVF. Therefore, we take advantage of the planar fault searched by the coseismic displacements of the foreshock, including GNSS and InSAR, to extend the CRF southwards to 22.9°N. Further south, we adopt the CRF previously proposed in the TEM[31]. Given the constraints from regional CMT solutions of the Chihshang sequence[30] and the aftershocks of the 2006 M_w 6.1 earthquake[27], we set the west-dipping angle of 60° for the CRF from 0 to 20 km depth in the model. On the other hand, the listric geometry of the LVF is well documented in the TEM[31]. The east-dipping angle gradually decreases from 75° at the surface to 45° at a depth of 20 km in our model. The fault geometry is discretized into parallelogram sub-faults approximately 2-km by 2-km in size, yielding 492 and 480 patches for the CRF and LVF, respectively.

To accommodate geodetic data with various temporal spans, we design an inversion scheme to simultaneously invert the coseismic slip during the foreshock and mainshock. The matrix form with linear observation equations for multiple geodetic data

is formulated as

$$\begin{bmatrix} \mathbf{d}_{D27} \\ \mathbf{d}_{A137} \\ \mathbf{d}_{S2} \\ \mathbf{d}_{G1} \\ \mathbf{d}_{G2} \end{bmatrix} = \begin{bmatrix} \mathbf{G}_{D27}^{CRF} & \mathbf{0} & \mathbf{0} & \mathbf{G}_{D27}^{R} & \mathbf{0} \\ \mathbf{G}_{A137}^{CRF} & \mathbf{G}_{A137}^{CRF} & \mathbf{G}_{A137}^{LVF} & \mathbf{0} & \mathbf{G}_{A137}^{R} \\ \mathbf{G}_{S2}^{CRF} & \mathbf{G}_{S2}^{CRF} & \mathbf{G}_{S2}^{LVF} & \mathbf{0} & \mathbf{0} \\ \mathbf{G}_{G1}^{CRF} & \mathbf{0} & \mathbf{0} & \mathbf{0} & \mathbf{0} \\ \mathbf{0} & \mathbf{G}_{G2}^{CRF} & \mathbf{G}_{G2}^{LVF} & \mathbf{0} & \mathbf{0} \end{bmatrix} \begin{bmatrix} \mathbf{m}_{fore}^{CRF} \\ \mathbf{m}_{main}^{CRF} \\ \mathbf{m}_{main}^{LVF} \\ \mathbf{m}_{D27}^{R} \\ \mathbf{m}_{A137}^{R} \end{bmatrix}$$

$$(2)$$

where each $\mathbf{G}$ is a matrix and each $\mathbf{d}$ and $\mathbf{m}$ are data and model vectors, respectively. The subscripts of $\mathbf{d}$ and $\mathbf{G}$ denote the data type (D27: ALOS-2 descending track 27; A137: ALOS-2 ascending track 137; S2: Sentinel-2; G1: GNSS of the foreshock; G2: GNSS of the mainshock). $\mathbf{m}$ and $\mathbf{G}$ with superscripts "CRF" or "LVF" represent the slip on the corresponding fault and the corresponding green's function. We assume an elastic half-space with a unified shear modulus of 30 GPa and a Poisson ratio of 0.25[50]. $\mathbf{m}$ with subscripts "fore" and "main" describes the fault slip during the foreshock and mainshock. Note that we limit the slip to south of Chihshang during the foreshock and north of 23°N during the mainshock to confine the slip distribution. In addition, we simultaneously fit a bilinear spatial ramp in the InSAR data to assimilate long-wavelength orbital errors that cannot be fully eliminated from data preprocessing. The super-script "R" on $\mathbf{m}$ and $\mathbf{G}$ stands for a ramp and the subscripts "D27" or "A137" refer to the corresponding InSAR image. In the inversion, we weight GNSS data according to their uncertainties, while InSAR data points are equally weighted. The relative weight between the InSAR and GNSS data is scaled to fit each dataset without a significant decrease of root-mean-square error (RMSE) to a specific data (Fig. S8), while the Sentinel-2 data is weighted one-tenth of the InSAR data due to the relatively large perturbations in the data (~10 times of the InSAR data).

Considering the sinistral oblique characteristics of the two faults, we perform non-negative least squares to penalize dextral-slip and normal faulting in the inverse problem. To avoid overfitting the data, we regularize the slip distribution on faults by

$$\mathbf{0} = \lambda_1 \begin{bmatrix} \mathbf{L}_{fore}^{CRF} & \mathbf{0} & \mathbf{0} \\ \mathbf{0} & \mathbf{L}_{main}^{CRF} & \mathbf{0} \\ \mathbf{0} & \mathbf{0} & \mathbf{L}_{main}^{LVF} \end{bmatrix} \begin{bmatrix} \mathbf{m}_{fore}^{CRF} \\ \mathbf{m}_{main}^{CRF} \\ \mathbf{m}_{main}^{LVF} \end{bmatrix} \tag{3}$$

where $\mathbf{L}$ is a discrete second-order Laplacian operator. The slip on the CRF and LVF share a unified hyperparameter λ_1. The hyperparameter λ_1 is determined by the trade-off curve between misfit and model roughness (Fig. S9). We also penalize the sum of the slip during the foreshock and mainshock individually by

$$\mathbf{0} = \lambda_2 \begin{bmatrix} \mathbf{1} & \mathbf{0} & \mathbf{0} \\ \mathbf{0} & \mathbf{1} & \mathbf{1} \end{bmatrix} \begin{bmatrix} \mathbf{m}_{fore}^{CRF} \\ \mathbf{m}_{main}^{CRF} \\ \mathbf{m}_{main}^{LVF} \end{bmatrix} \tag{4}$$

where $\mathbf{1}$ and $\mathbf{0}$ in the matrix are row vectors full of 1 and 0, respectively, and the hyperparameter λ_2 is the weight of the penalization. This is a weak penalization to suppress the slip on the subfaults with low resolution. The λ_1 and λ_2 adopted in our inverse model is 0.5 and 0.008, respectively. The RMSE of each dataset is documented in Table S1. The standard deviation of the slip model estimated by the model covariance is shown in Fig. S19.

The same approach is adopted to invert for the 34-day afterslip on the CRF and LVF with GNSS data (Fig. S15). To accommodate the broad postseismic displacements recorded by GNSS in western Taiwan, we extend the CRF down-dip to a depth of 30 km. It is worth mentioning that we do not penalize the early afterslip on the coseismic patches in our model. The

resulting model provides a RMSE of 9 mm for GNSS data (Fig. S16, Table S3).

Synthetic tests of the coseismic slip inversion. We performed a series of synthetic tests to evaluate the potential tradeoffs between the two faults (Fig. S18). We prepared the initial models by considering three scenarios, including (1) slip on the CRF during the foreshock and mainshock; (2) slip on the CRF and LVF during the foreshock and mainshock, respectively; and (3) slip on the CRF during the foreshock and on both the CRF and LVF during the mainshock. All the initial slip patches are limited within the depth of 10 km and characterized by 1 m of left-lateral and up-dip slip. We computed synthetic surface displacements at each geodetic data point, added noises according to the corresponding data uncertainties, and then inverted for the slip on the two faults using the same weights of data, regularization, and penalization adopted in our final inversion model. These results suggest that our model is indeed able to distinguish the slip on the CRF and LVF despite the spatial proximity of the two faults, giving us confidence in the performance of our model.

To verify whether the inverted slip on the LVF in our final model can be explained solely by the modeling artifacts caused by the slip on the CRF, we calculated the ratio of the inverted slip on the LVF to the inverted slip on the CRF in Synthetic test 1 (Fig. S18–1). This ratio represents the amount of inverted slip on the LVF that can be explained by modeling artifacts. We then compared the ratios estimated from Synthetic test 1 and our final inversion model. We first estimated the ratio using the mean slip on the two faults, resulting in 4% for strike-slip and 0.3% for dip-slip. The same estimation approach would yield 16% for strike-slip and 4% for dip-slip in our final inversion model, exceeding the baseline level predicted in Synthetic test 1. In other words, the slip on the LVF cannot be explained solely by modeling artifacts. We further estimated the ratio using the peak slip on the two faults. In Synthetic test 1, the ratio is 10% and 5% for strike-slip and dip-slip, respectively, while in our final inversion model, the ratio is 38% and 21%. Since these values are again greater than the baseline values predicted in Synthetic test 1, the inverted slip on the LVF is likely a robust feature. Moreover, a previous study indicates that the source models of the Chihshang mainshock independently inverted from teleseismic body waves, local strong motion, and GNSS data consistently show shallow slip on the LVF[32]. All these lines of evidence suggest that the Chihshang mainshock may be accompanied by a shallow slip on the LVF.

Kinematic rupture process inversion. The kinematic rupture model is analyzed based on the joint source inversion by considering both the GNSS coseismic static displacements and HR-GNSS data. All of the available HR-GNSS data, 50 s starting from the event origin time, were low-pass filtered at 0.5 Hz with a sampling rate of 1.0 s. Single-fault and dual-fault scenarios were tested for both the foreshock and the mainshock (Figs. S13–15, Table S2). A parallel Non-Negative Least-Squares[51] was applied to the joint inversion. The Green's functions of the GNSS data were calculated using the three-dimensional spectral-element method[52], where the local structure is taken as a 3D tomographic model[53]. Considering the 1 Hz sampling rate of HR-GNSS data, the synthetic Green's functions were low-pass filtered by 0.5 Hz and re-sampling to one point per second. There are 24 time windows of 0.8 s in length, and each window overlaps for 0.4 s. A maximum rupture speed of 3.0 km s^{-1} was assumed. Stability constraints were imposed, including damping at the edge of the fault and smoothing on both spatial and temporal slips on each subfault.

Coulomb stress estimation. We compute stress changes following the earthquakes with kernels that relate slip to stress changes[50]. The slip model of the 1951 earthquakes[16], and the 2022 foreshock and mainshock derived from this work serve as sources of stress changes in the computation. We first compute the stress changes induced by the 1951 earthquakes on the CRF (Fig. 5a). The rake of the CRF as a receiver fault is set to 45°, corresponding to a left-lateral oblique thrust fault. An effective friction coefficient of 0.4[54] on the receiver fault is adopted to scale the normal stress. Due to the geometrical discontinuity and overlapping in the 1951 model, some extreme values of stress changes on the CRF can be found, which are considered invalid. Then, we compute the stress changes on both the CRF and LVF induced by the foreshock of the 2022 sequence (Fig. 5b). Likewise, a rake angle of 45° is adopted for the LVF to approximate its left-lateral oblique behavior. Finally, we compute the total stress changes induced by the 2022 sequence, including the foreshock and mainshock, on both the CRF and LVF (Fig. 5c).

Convert Coulomb stress change to equivalent moment. Assuming the interaction between adjacent fault patches can be omitted, the relationship $\tau = K s_e$ can be used to obtain the first-order approximation between the stress change per unit area (τ in Pa) and the equivalent slip deficit (s_e in m). K stands for the stiffness that relates slip to stress (a wide range of 2–18 MPa m^{-1} estimated from our slip model, with fault dimensions ranging from the entire fault plane to a single slip patch). The equivalent slip deficit s_e is 0.03–0.5 m on the LVF during the 2022 earthquakes and 0.06–1 m on the CRF during the 1951 earthquakes. The equivalent moment can then be estimated by using $\mu A s_e$, where μ is the shear modulus and A is the affected area. For the equivalent moment decrease on the CRF caused by the 1951 earthquake, we adopt an average stress drop of 1 MPa ($s_e = 0.06$–0.50 m) and an affected area of 140-km × 30-km given the full rupture length of the LVF. The value is 7×10^{18}–6.3×10^{19} N·m, equivalent to the moment release from an M_w 6.5–7.1 earthquake. For the equivalent moment decrease on the LVF caused by the 2022 earthquake, we adopt an average stress drop of 0.5 MPa ($s_e = 0.03$–0.25 m) and an affected area of 60-km × 30-km given the segment length of the CRF that ruptured during this event. The value is 1.5×10^{18}–1.4×10^{19} N·m, equivalent to the moment release from an M_w 6.1–6.7 earthquake. The more conservative values (lower bounds) are used in Fig. 7b.

References

1. Ohta, Y. et al. Coseismic fault model of the 2008 Iwate-Miyagi Nairiku earthquake deduced by a dense GPS network. *Earth Planets Sp.* **60**, 1197–1201 (2008).
2. Zhang, X. et al. The 2018 MW 7.5 Papua New Guinea Earthquake: a dissipative and cascading rupture process. *Geophys. Res. Lett.* **47**, e2020GL089271 (2020).
3. Hamling, I. J. et al. Complex multifault rupture during the 2016 Mw 7.8 Kaikōura earthquake, New Zealand. *Science* **356**, eaam7194 (2017).
4. Pezzo, G. et al. Coseismic deformation and source modeling of the May 2012 Emilia (Northern Italy) earthquakes. *Seismol. Res. Lett.* **84**, 645–655 (2013).
5. Béon, M. L. et al. Shallow geological structures triggered during the Mw 6.4 Meinong earthquake, southwestern Taiwan. *Terr. Atmos. Ocean. Sci.* **28**, 663–681 (2017).
6. Yang, Y.-H. et al. Shallow slip of blind fault associated with the 2019 Ms 6.0 Changning earthquake in fold-and-thrust belt in salt mines of Southeast Sichuan, China. *Geophys. J. Int.* **224**, 909–922 (2021).
7. Stein, R. S., Lin, J. & King, G. C. P. Stress triggering of earthquakes: Evidence for the 1994 M = 6.7 Northridge, California, shock. *Ann. Geophys.* **37**, https://doi.org/10.1126/science.265.5177.1432 (1994).
8. Carena, S. & Suppe, J. Three-dimensional imaging of active structures using earthquake aftershocks: the Northridge thrust, California. *J. Struct. Geol.* **24**, 887–904 (2002).
9. Fuis, G. S. et al. Fault systems of the 1971 San Fernando and 1994 Northridge earthquakes, southern California: relocated aftershocks and seismic images from LARSE II. *Geology* **31**, 171–174 (2003).
10. Yeats, R. S. & Huftile, G. J. The Oak Ridge fault system and the 1994 Northridge earthquake. *Nature* **373**, 418–420 (1995).
11. Davis, T. L. & Namson, J. S. A balanced cross-section of the 1994 Northridge earthquake, southern California. *Nature* **372**, 167–169 (1994).
12. Dolan, J. F. et al. Prospects for larger or more frequent earthquakes in the Los Angeles metropolitan region. *Science* **267**, 199–205 (1995).
13. Dolan, J. F. & Rockwell, T. K. Paleoseismologic evidence for a very large (Mw>7), Post-A.D. 1660 surface rupture on the Eastern San Cayetano Fault, Ventura County, California: was this the elusive source of the damaging 21 December 1812 earthquake? *Bull. Seismol. Soc. Am.* **91**, 1417–1432 (2001).
14. Yeats, R. S. Late quaternary slip rate on the Oak Ridge fault, Transverse Ranges, California: Implications for seismic risk. *J. Geophys. Res.* **93**, 12137–12149 (1988).
15. Hsu, Y.-J., Yu, S.-B., Simons, M., Kuo, L.-C. & Chen, H.-Y. Interseismic crustal deformation in the Taiwan plate boundary zone revealed by GPS observations, seismicity, and earthquake focal mechanisms. *Tectonophysics* **479**, 4–18 (2009).
16. Chung, L.-H. et al. Seismogenic faults along the major suture of the plate boundary deduced by dislocation modeling of coseismic displacements of the 1951 M7.3 Hualien–Taitung earthquake sequence in eastern Taiwan. *Earth Planet Sci. Lett.* **269**, 416–426 (2008).
17. Chang, W.-Y., Chen, K.-P. & Tsai, Y.-B. An updated and refined catalog of earthquakes in Taiwan (1900–2014) with homogenized Mw magnitudes. *Earth Planets Sp.* **68**, 45 (2016).
18. Biq, C. The East Taiwan Rift. *Pet. Geol. Taiwan* **4**, 93–106 (1965).
19. Lee, J.-C. et al. Active fault creep variations at Chihshang, Taiwan, revealed by creep meter monitoring, 1998–2001. *J. Geophys. Res.* **108**, https://doi.org/10.1029/2003JB002394 (2003).
20. Shyu, J. B. H., Sieh, K., Chen, Y.-G. & Chung, L.-H. Geomorphic analysis of the Central Range fault, the second major active structure of the Longitudinal Valley suture, eastern Taiwan. *Geol. Soc. Am. Bull.* **118**, 1447–1462 (2006).
21. Lin, C.-W., Chen, W. S., Liu, Y. C. & Chen, P. T. Active faults in Eastern and Southern Taiwan. *Spec. Publ. Central Geol. Surv.* **23**, 1–10 (2009).
22. Omori, F. On the Bokusekikaku and Basshisho (Formosa) earthquake of January 11 1908. *Bull. Imp. Earth. Investig. Comm.* **2**, 156–165 (1908).
23. Cheng, S. N. & Yeh, Y. T. *Catalog of the earthquakes in Taiwan from 1604 to 1988.* (Academia Sinica, 1989).
24. Yu, S.-B. & Kuo, L.-C. Present-day crustal motion along the Longitudinal Valley Fault, eastern Taiwan. *Tectonophysics* **333**, 199–217 (2001).
25. Chen, H.-Y., Lee, J.-C., Tung, H., Chen, C.-L. & Lee, H. K. Variable vertical movements and their deformation behaviors at convergent plate suture: 14-year-long (2004–2018) repeated measurements of precise leveling around middle Longitudinal Valley in eastern Taiwan. *J. Asian Earth Sci.* **218**, 104865 (2021).
26. Chen, Y., Chen, K. H., Hu, J.-C. & Lee, J.-C. Probing the variation in aseismic slip behavior around an active suture zone: observations of repeating earthquakes in Eastern Taiwan. *J. Geophys. Res.* **125**, e2019JB018561 (2020).
27. Wu, Y.-M. et al. Seismogenic structure in a tectonic suture zone: with new constraints from 2006 Mw6.1 Taitung earthquake. *Geophys. Res. Lett.* **33**, https://doi.org/10.1029/2006GL027572 (2006).
28. Hsu, T. L. Recent faulting in the Longitudinal Valley of eastern Taiwan. *Mem. Geol. Soc. China* **1**, 95–102 (1962).
29. Shyu, J. B. H., Chung, L.-H., Chen, Y.-G., Lee, J.-C. & Sieh, K. Re-evaluation of the surface ruptures of the November 1951 earthquake series in eastern Taiwan, and its neotectonic implications. *J. Asian Earth Sci.* **31**, 317–331 (2007).
30. Lee, S.-J. et al. Towards real-time regional earthquake simulation I: real-time moment tensor monitoring (RMT) for regional events in Taiwan. *Geophys. J. Int.* **196**, 432–446 (2014).
31. Shyu, J. B. H., Yin, Y.-H., Chen, C.-H., Chuang, Y.-R. & Liu, S.-C. Updates to the on-land seismogenic structure source database by the Taiwan Earthquake

Model (TEM) project for seismic hazard analysis of Taiwan. *Terr. Atmos. Ocean. Sci.* **31**, 469–478 (2020).

32. Lee, S.-J., Liu, T.-Y. & Lin, T.-C. The role of the west-dipping collision boundary fault in the Taiwan 2022 Chihshang earthquake sequence. *Sci. Rep.* **13**, 3552 (2023).

33. Chen, W.-S. et al. A reinterpretation of the metamorphic Yuli belt: evidence for a middle-late Miocene accretionary prism in eastern Taiwan. *Tectonics* **36**, 188–206 (2017).

34. Lee, C.-P., Hirata, N., Huang, B.-S., Huang, W.-G. & Tsai, Y.-B. Evidence of a highly attenuative aseismic zone in the active collision orogen of Taiwan. *Tectonophysics* **489**, 128–138 (2010).

35. Tang, C.-H., Hsu, Y.-J., Barbot, S., Moore, J. D. P. & Chang, W.-L. Lower-crustal rheology and thermal gradient in the Taiwan orogenic belt illuminated by the 1999 Chi-Chi earthquake. *Sci. Adv.* **5**, eaav3287 (2019).

36. Hsu, Y.-J., Simons, M., Yu, S.-B., Kuo, L.-C. & Chen, H.-Y. A two-dimensional dislocation model for interseismic deformation of the Taiwan mountain belt. *Earth Planet. Sci. Lett.* **211**, 287–294 (2003).

37. Thomas, M. Y., Avouac, J.-P., Champenois, J., Lee, J.-C. & Kuo, L.-C. Spatiotemporal evolution of seismic and aseismic slip on the longitudinal Valley Fault, Taiwan. *J. Geophys. Res.* **119**, 5114–5139 (2014).

38. Thomas, M. Y., Avouac, J.-P., Gratier, J.-P. & Lee, J.-C. Lithological control on the deformation mechanism and the mode of fault slip on the longitudinal valley fault, Taiwan. *Tectonophysics* **632**, 48–63 (2014).

39. Brodsky, E. E. & van der Elst, N. J. The uses of dynamic earthquake triggering. *Annu. Rev. Earth Planet. Sci.* **42**, 317–339 (2014).

40. Cruz-Atienza, V. M. et al. Short-term interaction between silent and devastating earthquakes in Mexico. *Nat. Commun.* **12**, 2171 (2021).

41. Dolan, J. F., Bowman, D. D. & Sammis, C. G. Long-range and long-term fault interactions in Southern California. *Geology* **35**, 855–858 (2007).

42. Mildon, Z. K. et al. Surface faulting earthquake clustering controlled by fault and shear-zone interactions. *Nat. Commun.* **13**, 7126 (2022).

43. Shyu, J. B. H., Sieh, K., Avouac, J.-P., Chen, W.-S. & Chen, Y.-G. Millennial slip rate of the Longitudinal Valley fault from river terraces: Implications for convergence across the active suture of eastern Taiwan. *J. Geophys. Res.* **111**, https://doi.org/10.1029/2005JB003971 (2006).

44. Yen, I.-C. et al. Paleoseismological study on the Chihshang segment of the longitudinal valley fault in eastern Taiwan. *Spec. Publ. Central Geol. Surv.* **28**, 43–70 (2014).

45. Leprince, S., Barbot, S., Ayoub, F. & Avouac, J. P. Automatic and precise orthorectification, coregistration, and subpixel correlation of satellite images, application to ground deformation measurements. *IEEE Trans. Geosci. Remote Sens.* **45**, 1529–1558 (2007).

46. Liang, C., Liu, Z., Fielding, E. J. & Bürgmann, R. InSAR time series analysis of L-Band Wide-Swath SAR Data Acquired by ALOS-2. *IEEE Trans. Geosci. Remote Sens.* **56**, 4492–4506 (2018).

47. Bertiger, W. et al. GipsyX/RTGx, a new tool set for space geodetic operations and research. *Adv. Sp. Res.* **66**, 469–489 (2020).

48. Boehm, J., Werl, B. & Schuh, H. Troposphere mapping functions for GPS and very long baseline interferometry from European Centre for Medium-Range Weather Forecasts operational analysis data. *J. Geophys. Res.* **111**, https://doi.org/10.1029/2005JB003629 (2006).

49. Barbot, S., Fialko, Y. & Bock, Y. Postseismic deformation due to the Mw 6.0 2004 Parkfield earthquake: Stress-driven creep on a fault with spatially variable rate-and-state friction parameters. *J. Geophys. Res.* **114**, https://doi.org/10.1029/2008JB005748 (2009).

50. Nikkhoo, M. & Walter, T. R. Triangular dislocation: an analytical, artefact-free solution. *Geophys. J. Int.* **201**, 1119–1141 (2015).

51. Lee, S.-J. et al. Source complexity of the 4 March 2010 Jiashian, Taiwan, Earthquake determined by joint inversion of teleseismic and near field data. *J. Asian Earth Sci.* **64**, 14–26 (2013).

52. Komatitsch, D. et al. Simulations of ground motion in the Los Angeles Basin based upon the spectral-element method. *Bull. Seismol. Soc. Am.* **94**, 187–206 (2004).

53. Huang, H.-H. et al. Investigating the lithospheric velocity structures beneath the Taiwan region by nonlinear joint inversion of local and teleseismic P wave data: slab continuity and deflection. *Geophys. Res. Lett.* **41**, 6350–6357 (2014).

54. Hsu, Y.-J., Rivera, L., Wu, Y.-M., Chang, C.-H. & Kanamori, H. Spatial heterogeneity of tectonic stress and friction in the crust: new evidence from earthquake focal mechanisms in Taiwan. *Geophys. J. Int.* **182**, 329–342 (2010).

55. Wu, Y.-M., Chang, C.-H., Zhao, L., Teng, T.-L. & Nakamura, M. A comprehensive relocation of earthquakes in Taiwan from 1991 to 2005. *Bull. Seismol. Soc. Am.* **98**, 1471–1481 (2008).

56. Tang, C.-H. et al. Geodetic dataset and slip models of the 2022 Chihshang earthquake sequence in eastern Taiwan, https://doi.org/10.5281/zenodo.8268096 (2023).

57. Hsu, Y.-J., Yu, S.-B. & Chen, H.-Y. Coseismic and postseismic deformation associated with the 2003 Chengkung, Taiwan, earthquake. *Geophys. J. Int.* **176**, 420–430 (2009).

58. Lee, S.-J., Huang, H.-H., Shyu, J. B. H., Yeh, T.-Y. & Lin, T.-C. Numerical earthquake model of the 31 October 2013 Ruisui, Taiwan, earthquake: source rupture process and seismic wave propagation. *J. Asian Earth Sci.* **96**, 374–385 (2014).

59. Lee, S. J., Lin, T. C., Liu, T. Y. & Wong, T. P. Fault-to-fault jumping rupture of the 2018 Mw 6.4 Hualien earthquake in eastern Taiwan. *Seismol. Res. Lett.* **90**, 30–39 (2018).

60. Lee, S.-J., Wong, T.-P., Liu, T.-Y., Lin, T.-C. & Chen, C.-T. Strong ground motion over a large area in northern Taiwan caused by the northward rupture directivity of the 2019 Hualien earthquake. *J. Asian Earth Sci.* **192**, 104095 (2020).

61. Jian, P.-R. & Wang, Y. Applying unsupervised machine-learning algorithms and MUSIC back-projection to characterize 2018–2022 Hualien earthquake sequence. *Terr. Atmos. Ocean. Sci.* **33**, 28 (2022).

Acknowledgements

Author contributions

C.-H.T., Y.N.L., Y.W., S.-J.L., and Y.-J.H. conducted the study and wrote the manuscript with the contributions from all other coauthors. J.B.H.S. and Y.W. carried out the field survey. H.T. and H.-Y.C processed the GNSS data. Y.N.L. and Y.-T.K. processed the ALOS-2 and Sentinel-2 data. S.-J.L. performed the kinematic rupture process inversions. C.-H.T. performed the static coseismic and postseismic slip inversions, Coulomb stress calculations, and historical seismicity analysis. All authors contributed to the discussion and interpretation of the results.

Competing interests

The authors declare no competing interests.

Additional information